Evaluating metal oxide support effects on the RWGS activity of Mo_2C catalysts

Journal:	*Catalysis Science & Technology*
Manuscript ID	CY-ART-01-2023-000026.R1
Article Type:	Paper
Date Submitted by the Author:	22-Mar-2023
Complete List of Authors:	Holder, Cameron; US Naval Research Laboratory, Materials Science and Technology Division Morse, James; US Naval Research Laboratory, Materials Science and Technology Division Barboun, Patrick; US Naval Research Laboratory Shabaev, Andrew; US Naval Research Laboratory, Materials Science and Technology Division Baldwin, Jeffrey; US Naval Research Laboratory, Acoustics Division Willauer, Heather; Naval Research Laboratory, Materials Science and Technology Division

ARTICLE

Evaluating metal oxide support effects on the RWGS activity of Mo_2C catalysts†

Received 00th January 20xx,
Accepted 00th January 20xx

DOI: 10.1039/x0xx00000x

Cameron F. Holder*[a], James R. Morse[a], Patrick M. Barboun[b], Andrew R. Shabaev[a], Jeffrey W. Baldwin[c], Heather D. Willauer[a]

The reverse water gas shift reaction (RWGS) is an important first step in the thermochemical transformation of CO_2 to fuels. Recent research efforts have investigated transition metal carbides due to their high activity and terrestrial abundance. In order to improve particle dispersion and mechanical stability, the catalysts are often deposited onto high surface area metal oxide supports. Understanding the influence the oxide support has on the observed catalytic activity is imperative for increased efficiency. Herein, we investigate the effect of the oxide support's (γ-Al_2O_3, SiO_2, ZrO_2, CeO_2, and MgO) reducibility and acidity on potassium promoted molybdenum carbide catalysts for the RWGS. Additionally, DFT computation was used to evaluate CO and CO_2 adsorption energies at a model interface of Mo_2C/MgO. It is demonstrated that non-reducible and acidic supports are the most active for the production of CO with K-Mo_2C/Al_2O_3 showing the highest CO site time yield of 55.6 min^{-1}.

Introduction

The limited supply of non-renewable energy sources, coupled with the current lack of renewable energy infrastructure, have prompted research efforts to establish alternative methods to produce hydrocarbon fuels and chemicals.[1–6] A potential avenue towards achieving renewable fuel and chemical production is through the recycling and conversion of CO_2 via electrochemical and/or thermal processes.[6–8] Furthermore, efficient CO_2 capture and utilization is becoming increasingly prioritized by the U.S. DoD as it moves towards developing methods to generate fuel "near or at the point of use" which will both assist in the development of climate-resilient supply chains and offer significant logistical, operational, and cost advantages.[9,10] To address this, the Naval Research Laboratory has recently developed a method that electrolytically extracts CO_2 from seawater while simultaneously produces H_2. These gases can be subsequently used as feedstocks for the thermocatalytic production of fuel.[11–17]

An important reaction in the overall utilization of CO_2 is its reduction to CO via the RWGS reaction (Equation 1), as the product CO can be further reduced to longer chain hydrocarbons through the Fischer-Tropsch synthesis. The RWGS reaction, being endothermic, is equilibrium-limited such that higher temperatures drive the reaction towards higher conversions. For instance, the equilibrium conversion of CO_2 to CO at 300 °C for a 3:1 H_2:CO_2 blend is ~23 % while an increase in temperature to 600 °C results in CO_2 conversions of ~60 %.[18] While large CO_2 conversions can thus be achieved with elevated temperatures, this also requires greater energy inputs which often result in accelerated deactivation of the catalyst and constrains the design and operation of the reactor.[16,19–22] While lower operating temperatures can help mitigate these negative consequences, decreased conversion rates due to equilibrium limitations, as well as competing reactions such as CO_2 methanation (Equation 2), reduce the reaction efficiency.[23,24] This emphasizes the need for RWGS catalysts that provide both high activity and high CO selectivity over a range of operating temperatures in order to most efficiently utilize the CO_2 and H_2 precursors.

$$\mathrm{CO_2 + H_2 \rightleftharpoons CO + H_2O} \tag{1}$$

$$\mathrm{CO_2 + 4H_2 \rightarrow CH_4 + 2H_2O} \tag{2}$$

Noble metals and noble metal containing alloys such as Pt, Pd, Pt-Co, and Pd-In among many others have been shown to be active catalysts for the RWGS reaction though the use of these materials on larger scales is prohibited by cost.[25–28] Research efforts have thus focused on finding alternatives to noble metal catalysts. Recently, transition metal carbides, such as molybdenum and tungsten, have attracted significant attention, as they exhibit activity that mimics the activity of noble metals for a variety of catalytic reactions.[29–31] For example, Mo_2C has been reported as a catalyst for many reactions including CO_2 hydrogenation,[32,33] methane reforming and aromatization,[34–37] the hydrogen evolution reaction,[38,39] and the RWGS reaction.[16,30] In particular, Porosoff et al.

---

[a] Materials Science and Technology Division, Naval Research Laboratory, Washington, D.C. 20375, USA.
[b] NRC Postdoctoral Research Associate, Naval Research Laboratory, Washington, D.C. 20375, USA.
[c] Acoustics Division, Naval Research Laboratory, Washington, D.C. 20375, USA.

†Electronic Supplementary Information (ESI) available: [details of any supplementary information available should be included here]. See DOI: 10.1039/x0xx00000x

reported that potassium promoted Mo_2C supported on γ-alumina was an excellent catalyst for the RWGS reaction, demonstrating a CO_2 conversion of 18.1% at 300 °C and 19.4 bar with a CO selectivity of 95.9%.[16] Additionally, Morse et al. demonstrated that alkali promoted WC supported on γ-Al_2O_3 exhibited a CO_2 conversion of 20.3% while still maintaining a high CO selectivity of 98.1% at 350 °C.[17]

High surface area oxide supports, such as silica and alumina, are commonly used in thermo-catalytic processes to generate well dispersed catalysts with large active surface areas, and can help to improve the thermal and mechanical stability of the catalyst. Additionally, the chemical nature of the support, and its interaction with the catalytic material, can also influence both the catalytic mechanism and the catalyst performance.[40–43] For instance, Pt and Cu that are deposited onto reducible oxides, such as CeO_2 and TiO_2, often exhibit improved turnovers for the RWGS when compared to the same catalyst deposited onto non-reducible oxides such as Al_2O_3. This improvement is often attributed to the production of oxygen vacancies that emerge from the reduction of metal cations in the support due to the H_2 reactant. The adsorption of CO_2 to the oxygen vacancy reoxidizes the support and simultaneously generates CO, closing the catalytic cycle.[44–48] In addition to reducibility, acidic or basic sites on the support can also significantly affect the catalytic conversion and selectivity.[49–53] Juneau et al. recently demonstrated that Mo_2C supported on aluminosilicate zeolites with various Si/Al ratios were highly dependent on the Lewis acid site density, with larger densities being correlated to larger CO yields.[53] Furthermore, Sakurai et al. showed that the product selectivity for CO_2 reduction on Au catalysts could be controlled to produce either methanol or CO depending on whether a basic or acidic support was used.[54] While the influence of catalyst support has been studied for pure metals and metallic alloys, support interactions with carbide catalysts, specifically for the RWGS reaction, has received considerably less attention.

Herein, we report the activity of potassium promoted Mo_2C supported on various metal oxides to investigate the influence of support reducibility and acidity on the CO site time yields and product selectivity for the RWGS reaction. We show that K-Mo_2C is significantly more active when supported on non-reducible supports such as γ-Al_2O_3 when compared to reducible supports like CeO_2. The observed activity also correlated well with the support acidity with more acidic supports exhibiting higher CO site time yields.

Experimental

Materials

All chemicals were used as purchased without further purification. Ammonium molybdate tetrahydrate (99.98%), potassium carbonate (99.0%), zirconium(IV) oxide (ZrO_2, nanopowder), magnesium oxide (MgO, 99.0%), cerium(IV) oxide (CeO_2, >99.95%), titanium dioxide (TiO_2, 325 mesh), and silicon(IV) dioxide (SiO_2, 200-400 mesh) were purchased from Sigma-Aldrich. Aluminum oxide (γ-Al_2O_3, 97%) was purchased from Strem Chemicals. The catalytic reactors utilized a packed bed configuration and were made from 1/4” 316L stainless steel tubing purchased from Swagelok. Gases including hydrogen (99.999%), nitrogen (99.9995%), and carbon dioxide (99.5%), were purchased through Earlbeck Gasses and Technology while UHP methane (99.97%) was purchased through Matheson.

Catalyst Preparation

Catalysts were prepared using an evaporation deposition method. For all catalyst materials, the weight percentages of K and Mo were 2% and 19%, respectively. To accomplish this, 4.70 g of ammonium molybdate tetrahydrate and 0.48 g of potassium carbonate were dissolved in 200 mL of DI water under constant stirring. Once dissolved, 10 g of the support powder was added to the stirring solution and left to evaporate overnight at 90 °C. The dry powder was homogenized with a mortar and pestle before being loaded into alumina crucibles and calcined in air to form molybdenum oxides at temperatures ranging from 350-600 °C depending on the support.

The calcined powders were ground with a mortar and pestle before approximately 1.0 g of the powder was transferred into an aluminum crucible boat. The impregnated and calcined powder was then carburized under flowing CH_4 and H_2 at temperatures ranging from 650 to 750 °C depending on the support. The flowrates of CH_4 and H_2 were 60 and 240 mL/min, respectively. Gas chromatography was used to monitor reaction progress via the evolution of CO gas. Upon the loss of CO signal, the furnace was cooled to 600 °C, the CH_4 flowrate was shut off, and the supported catalysts were treated under flowing H_2 for 1 hour to remove deposited carbon. After an hour under flowing H_2, the furnace was cooled to room temperature and the surface was passivated for a minimum of one hour with a stream of 1% O_2/N_2 flowing at 10 mL/min.

Catalyst Testing

Prior to catalytic testing, the carburized powders were pressed into pellets and then sieved to obtain a powder with particle sizes ranging between 255 and 315 µm. A ¼” stainless steel reactor was loaded with 0.335 g of the size-selected carburized catalyst with glass wool acting as plugs at both ends. The catalyst bed was reduced for 90 minutes at 300 °C and 6.9 bar of H_2 which was set at a flowrate of 50 mL/min. The pressure was then increased to 19.3 bar with a mixture of N_2, H_2, and CO_2 where the ratio of H_2:CO_2 was 3:1 and N_2, used as an internal standard, comprised 16.5% of the gaseous mixture. Gaseous flowrates were controlled using programmable Brooks Mass Flow controllers and the total flowrate was varied depending on the desired WHSV. The reactor effluent was passed through a cold trap set at 5 °C in order to remove any water prior to GC characterization. The effluent reactor stream was monitored by an Agilent 7890A online gas chromatograph and all data reported herein were collected after steady state conditions had been reached. Carbon balances between 95% and 100% were observed for all reported reactor data.

Materials Characterization

Scanning electron microscopy (SEM) was performed using a Carl Zeiss Supra 55 microscope equipped with Schottky thermal field emission. Images were obtained at an accelerating voltage of 3 keV with an average working distance of 7 mm and a 30 µm aperture. X-ray energy dispersive spectroscopy (EDS) maps were obtained using a Princeton Gamma Tech EDS detector at accelerating voltages of 10 keV and working distance of 15 mm.

Powder X-ray diffraction (XRD) patterns were obtained using a Rigaku Smartlab X-ray diffractometer using Cu Kα radiation (λ = 1.5406 nm) over a 2Θ range of 10–80°. Experimental patterns were analyzed and compared to reference patterns using the Rigaku PDXL software. The peak representing the (1-11) plane of Mo_2C was chosen for Scherrer analysis as there are no overlapping support peaks on any studied material located around 39.4° 2Θ.

All thermogravimetric analysis and mass spectrometry (TGA-MS) experiments were performed using a TA Instrument Q500 TGA that was coupled to a Hiden Analytical HPR-20 benchtop mass spectrometer. Approximately 50 mg of sample was added for each analysis. Nitrogen was used as the purge gas, flowing at a rate of 200 mL/min. Each run was comprised of a 30-minute equilibration stage at room temperature before the sample was heated to 750 °C at a rate of 5 °C/min. The products released from the sample during heating were monitored in real-time by mass spectrometry over a m/z range of 2-120. All ions were detected using an ionization energy of 70 eV. The TGA spectra were analyzed using the TA Universal software while the mass spectra were analyzed using the EGAsoft package.

BET surface area analysis was conducted through N_2 adsorption experiments using a Beckman-Coulter S.A. 3100 Surface Area Analyzer. Prior to the experiment, all powders were degassed at 120 °C for 15 minutes under vacuum. All surface area analyses were conducted in liquid N_2 (-196 °C).

CO pulse chemisorption experiments were run using a Micromeritics Autochem II equipped with a thermal conductivity detector. Approximately 150 mg of catalyst were loaded into a quartz U-tube containing a plug of glass of wool. The sample was heated under H_2 to 300 °C for 1.5 hours to mirror the pre-treatment catalytic conditions. After 1.5 hours, the gas flow was changed to helium and the sample was allowed to cool to room temperature. Once at room temperature, the furnace was removed and the quartz tube was submerged into a dewar containing a dry-ice/iso-propanol bath (~ -70 °C). Once the temperature had stabilized, CO pulse chemisorption experiments were started using He as a reference gas flowing at 50 mL/min. In total, 10 pulses of 10% CO/He were introduced over the sample with 5 minutes programmed in between each pulse where the sample loop had a volume of 0.035 cm^3. The total amount of CO absorbed was then used to calculate the amount of active Mo sites assuming that one molecule of CO absorbed to one active Mo site.[55,56]

Temperature programmed oxidation and temperature programmed desorption experiments were conducted using a Micromeritics Autochem II equipped with a thermal conductivity detector and mass spectra were obtained using a Hiden Analytical HPR-20 benchtop mass spectrometer. Approximately 100 mg of catalyst powder was loaded into a quartz U-tube that was plugged with glass wool. The sample was heated to 300 °C under flowing H_2 for 1 hour to mirror the pre-treatment catalytic conditions. For the TPD experiments, CO_2 was flowed over the catalyst for 1 hour, before He was introduced and the temperature was ramped to 300 °C. For the TPO experiments, a 10% blend of CO_2 in He was introduced and the sample was allowed to equilibrate for minutes before being heated to 350 °C. The collected mass spectra were analyzed using the EGAsoft package.

Computation Modelling

Calculations were performed using the Vienna ab initio Simulation Package (VASP).[57] The Perdew-Burke-Ernzerhof (PBE) generalized gradient approximation was employed as the electron exchange correlation functional using the PBE projector augmented-wave (PAW) potentials.[58,59] The electronic energy threshold was set at 10^{-6} eV while the ionic force threshold was set at 0.02 eV $Å^{-1}$. While hybrid functionals are widely utilized to model both semiconductors and insulators, the use of these functionals were not employed for this study due to the metallic nature of Mo_2C.All calculations used the Monkhorst-Pack k-points mesh sampling where the bulk slabs utilized a k-point grid of 3 x 3 x 1 while the Mo_2C ribbon supported on MgO utilized a k-point grid of 1 x 3 x 1.[60]

The lattice parameters of the orthorhombic Mo_2C unit cell were 4.743 x 6.058 x 5.231 Å where each unit cell contained 12 atoms arranged in 2 Mo layers (4 Mo in each layer) and 2 C layers (2 atoms in each layer). The bulk slab of $Mo_2C(100)$ was composed of 8 unit cells arranged in a (2 x 2) supercell with dimensions of 9.486 x 12.116 x 10.461 Å and a total of 96 atoms. This slab was optimized and relaxed with a vacuum space of 58.0 Å. Meanwhile, the slab of MgO(111) was terminated on both sides by oxygen to mitigate the inherent polarity of the (111) facet. The (2 x 2) supercell of MgO(111). had dimensions in the a and b directions of 10.318 and 11.914 Å, respectively. In the c direction, the MgO(111) slab was 12 layers thick, or 6 unit cells composed of alternating layers of Mg and O with a vacuum space of 53.2 Å.

A simple model of Mo_2C/MgO was developed by using the optimized MgO(111) and $Mo_2C(100)$ slabs described above with slight adjustments to the Mo_2C slab. These two surfaces were initially chosen because of the good overlap between the lattice parameters which would help mitigate any large atomic rearrangements. Firstly, the (2 x 2) $Mo_2C(100)$ supercell was rotated such that it was aligned with the MgO(111) surface. Additionally, one carbon layer (8 atoms) was removed from one side of the Mo_2C supercell such that the film was terminated by Mo on both sides resulting in a slab with a total of 88 atoms. The slabs were then modelled such that the vacuum distance between the two films was approximately 18 Å. The overall structure was composed of 264 atoms (96 magnesium, 80 oxygen, 24 carbon, and 64 molybdenum) and had unit dimensions of 11.987 x 10.381 x 65 Å. The vacuum gap between

Table 1 Calcination and carburization temperatures, average Mo_2C particle size, and BET surface areas with and without K-Mo_2C for each support.

	Calcination Temperature (°C)	Carburization Temperature (°C)	Particle Size (nm)	BET Surface area w/out Mo_2C (m^2/g)	BET Surface area w/ Mo_2C (m^2/g)
Al_2O_3	350	650	7	201.5	116.1
SiO_2	450	700	12	409.4	195.8
ZrO_2	600	750	23	32.2	14.9
CeO_2	650	725	28	31.0	3.6
MgO	450	750	21	29.6	18.8

the two films was then decreased to 1.8 Å while the vacuum gap on the other side of the structure was increased to 44.5 Å to preserve the z-axis unit dimension of 65 Å. All atoms in the Mo_2Clayer were allowed to relax along with top two layers of the MgO surface and the final separation distance between the two slabs after relaxation was approximately 1.5 Å. The ribbon of Mo_2C supported on MgO was then generated by removing half of the Mo_2C slab which resulted in a (1 x 2) Mo_2C supercell on the surface of MgO(111). Molecules of CO_2 and CO were placed at various positions on the surface of both Mo_2C(100) and the oxygen-terminated MgO(111) to determine the optimal adsorption sites for each molecule. Additionally, for the Mo_2C ribbon supported on MgO, molecules of CO_2 and CO were placed parallel to the Mo_2C ribbon and approximately 2 Å above the surface. These structures were allowed to relax and the adsorption energies were calculated by the following: $E_{ads} = E_{slab+molecule} - E_{molecule} - E_{slab}$.

Results and Discussion

Synthesis and Characterization

The selected calcination temperatures for each material were determined through TGA-MS and are reported in Table 1. For instance, mass loss associated with oxidation of the molybdate precursor was observed at temperatures upwards of 610 °C for CeO_2 but only 400 °C for MgO. As such, the calcination temperatures reported in Table 1 were chosen to be slightly greater than those observed by TGA-MS to ensure the complete oxidation of the molybdate precursors. The range of temperatures reported indicates that the support influences the oxidation of the molybdenum precursor. The XRD patterns of the materials post-calcination but prior to the carburization process are shown in Fig. S1. The formation of a variety of different molybdenum mixed-metal oxides are readily observed and the various phases that were formed are tabulated in Table S1.

After oxidation, the supported catalysts were then carburized at elevated temperatures with a 4:1 blend of H_2:CH_4 to transform the molybdenum oxides into Mo_2C. The carburization temperature for each catalyst was determined by monitoring the effluent stream for CO using online gas chromatography. To determine the carburization temperature required for the respective catalyst/support combinations, the temperature was initially set at 650 °C, then ramped every 45 minutes at intervals of 25 °C until a CO signal was observed, indicating the formation of Mo_2C.[61,62] The carburization temperatures applied for each catalyst/support combination are also shown in Table 1. Directly following the carburization step, all samples except for the K-Mo_2C/CeO_2 were treated at 600 °C under flowing H_2 to remove any excess carbon that may have deposited.[16] It was found that upon subjection to this H_2 treatment step, the K-Mo_2C/CeO_2 sample was partially reduced from Mo_2C to metallic Mo (Fig. 1). When reducible oxide supports are exposed to reducing environments at elevated temperatures, the metal cations are often reduced which can ultimately promote electron transfer from the support to the deposited metal. The electronic contributions from the strong metal support interaction (SMSI) can thus help to rationalize the observed reduction of Mo_2C to Mo on CeO_2 upon exposure to H_2 at elevated temperatures.[63–66]

Experimental XRD patterns (colored) for the supported K-Mo_2C materials along with the corresponding metal oxide reference patterns (gray) are presented in Fig. 1. All samples showed sharp peaks that are indicative of highly crystalline Mo_2C, denoted by asterisks, along with signatures corresponding to the respective metal oxide supports. Due to the amorphous nature of silica, no reference pattern is included for the SiO_2 support. While the asterisks shown in Fig. 1 denote an orthorhombic Mo_2C (β-Mo_2C) reference pattern, the presence of hexagonal Mo_2C (α-Mo_2C) cannot be entirely dismissed due to the challenge of selectively synthesizing one particular phase as well as similarities in the reference XRD

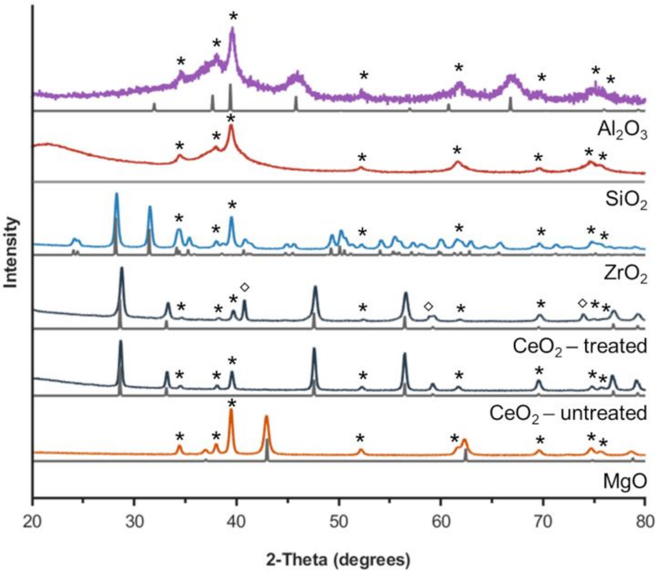

Fig. 1 Experimental XRD patterns showing K-Mo2C supported on Al2O3, SiO2, ZrO2, CeO2, and MgO. The grey patterns represent the corresponding metal oxide reference patterns while the diamonds and *3 represent metallic Mo and Mo2C peaks, respectively.

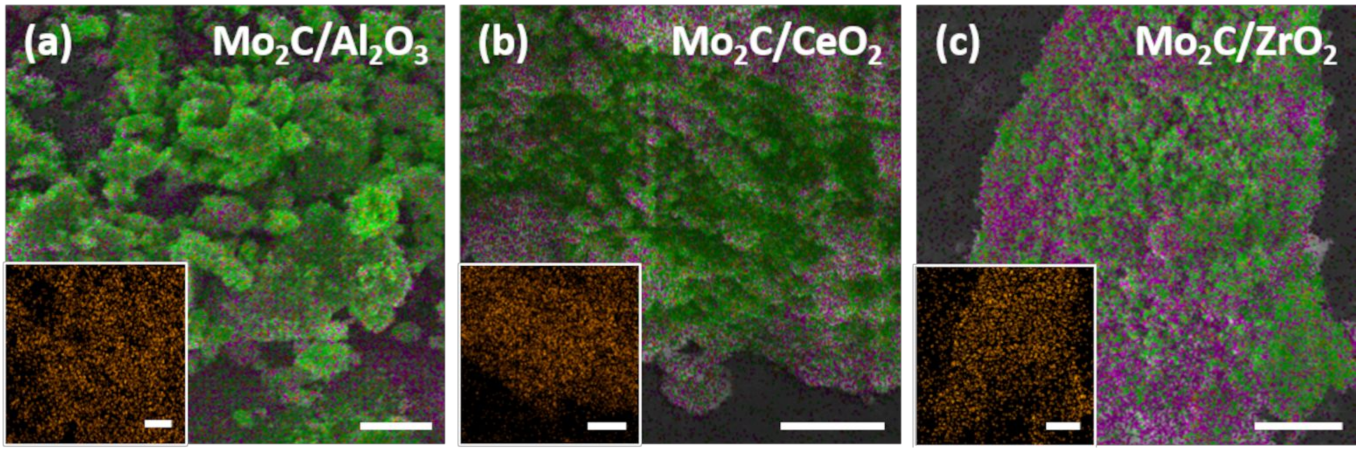

Fig. 2 Overlaid SEM/EDS maps of Mo2C supported on a) Al2O3, b) CeO2, and c) ZrO2 where green represents Mo and purple represents the support metal (Al, Ce, or Zr). The potassium elemental maps are shown in orange in the insets for each image. The scale bars represent 2 μm.

reference patterns for α- and β-Mo_2C. Though β-Mo_2C is more extensively studied, both phases have been shown to be catalytically active.[67,68] The lack of XRD peaks corresponding to any MoO_x or bimetallic oxide species indicated that the selected temperatures for carburization were appropriate to achieve complete conversion to the desired Mo_2C phase for all of the supported catalysts. Additionally, the XRD patterns showed that the reduction of the deposited carbon at 600 °C, with the exception of CeO_2, did not significantly reduce the bulk Mo_2C phase to metallic Mo. Experiments to synthesize K-Mo_2C supported on TiO_2 were also attempted using calcination and carburization temperatures of 350 °C and 750 °C, respectively. However, the experimental XRD pattern (Fig. S2) indicated a mixed-phase population with phases such as Mo_2C and various oxides including titanium molybdates and potassium titanates. The presence of the impurity oxides is most likely attributed to both the mobility of the oxygen vacancies in TiO_2 as well as the increased diffusion rate of the deposited metals at elevated temperatures.[69–71]

The Mo_2C crystallite sizes were calculated from the experimental XRD patterns using the Scherrer equation and can be seen in Table 1. The smallest calculated Mo_2C size was 7 nm which corresponded to Mo_2C deposited on γ-Al_2O_3. CeO_2 had the largest calculated Mo_2C size of 28 nm. The other supports including SiO_2, MgO, and ZrO_2 showed calculated Mo_2C particle sizes of 12, 21, 22, and 23 nm, respectively. The surface areas for both the unloaded and loaded supports were determined by BET analysis and the results are also presented in Table 1. The measured surface area of the loaded and carburized supports decreased by approximately 50% when compared to bare supports without metal loading. In particular, CeO_2 exhibited a more drastic change, exhibiting nearly a 10-fold drop in the measured surface area which is most likely due to the ripening of the Mo_2C particles. In general, the calculated particle size of Mo_2C was inversely correlated with the measured BET surface area. This result is intuitive as high surface area supports tend to produce smaller particles due to the increased amount of surface sites available for nucleation.

To determine the distribution of potassium and molybdenum on the support post-carburization, the materials were further characterized by SEM-EDS. Representative elemental maps for K-Mo_2C on select supports are shown in Fig. 2. The potassium maps (Insets, Fig. 2) demonstrate that potassium was homogenously distributed with no large aggregates being detected. In contrast, molybdenum tended to aggregate in particular areas on each support. The large difference between the agglomerate sizes observed in the SEM-EDS micrographs and the small particle sizes calculated by the Scherrer equation indicates that the Mo_2C is either polycrystalline or composed of smaller Mo_2C particles which are beneath the resolution limit of the SEM.

Catalytic Results

For a typical catalytic experiment, the catalyst bed was exposed to a flowing blend of 3:1 H_2:CO_2 at 300 °C, and a pressure of 19.3 bar. The CO_2 conversions and product selectivity for K-promoted Mo_2C deposited on various metal oxide supports are presented in Fig. 3 at a WHSV of 2 mL s^{-1} g^{-1}. Under these conditions, the K-promoted Mo_2C/Al_2O_3 catalyst demonstrated the highest CO_2 conversion at 18.2% with a selectivity towards CO of 95.2% and the remaining balance composed of CH_4. This result aligns well with prior reports that also show high CO_2 conversions for Mo_2C and a significant increase in CO selectivity with the use of alkali metal promoters such as potassium. K-promoted Mo_2C supported on ZrO_2 and

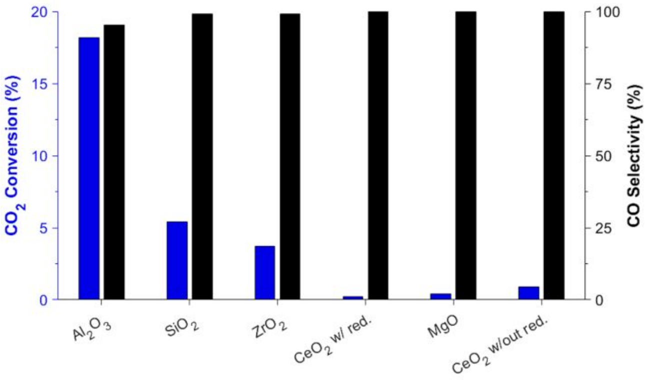

Fig. 3 CO_2 conversion (blue) and CO selectivity (black) of K-promoted Mo_2C supported on various metal oxides at a WHSV of 2 mL s^{-1} g^{-1}.

SiO_2 were also found to be active with CO_2 conversions of 5.4% and 3.7%, respectively with 99.1% and 99.2% CO selectivity, respectively. K-Mo_2C/CeO_2 that was not treated with H_2 directly following carburization showed slightly lower conversions than K-Mo_2C/CeO_2 that was treated with H_2 though both conversions, along with MgO, were <1%, albeit with no observed methane production. The reduced conversion over the untreated K-Mo_2C/CeO_2 is attributed carbon leftover from the carburization process that is blocking active sites while the low conversions over the treated K-Mo_2C/CeO_2 is attributed to the presence of Mo metal which is inactive for the RWGS.[72]

In order to compare the intrinsic activity of Mo_2C on different supports, CO pulse chemisorption was used to determine the number of Mo active sites per gram of material which was then used to calculate the CO site time yield (STY). The results of the CO pulse chemisorption experiments can be seen in Table 2. K-Mo_2C supported on CeO_2 that was subjected to the H_2 treatment was calculated to have the greatest density of Mo active sites at 5.6 μmol/g. However, this is likely an overestimate compared to the true quantity of catalytically active sites as metallic Mo, which is inactive for the RWGS reaction, is also known to adsorb CO under these conditions.[56] For that reason, this sample was omitted from Table 2. Comparatively, the K-Mo_2C/CeO_2 that was not exposed to the H_2 treatment and thus exhibited no detectable metallic Mo by XRD, was calculated to have a Mo active site density of 0.8 μmol/g. Meanwhile, active site densities for K-Mo_2C supported on γ-Al_2O_3 and SiO_2 were 5.6 and 2.9 μmol/g, respectively. Furthermore, K-Mo_2C supported on ZrO_2 and MgO had active site densities of 2.0 and 0.7 μmol/g, respectively.

Table 2 Mo active sites (μmol/g) determined by CO pulse chemisorption and the CO STY (min^{-1}).

	Mo active sites (μmol/g)	CO STY (min^{-1})
Al_2O_3	5.6	55.6
SiO_2	2.9	23.3
ZrO_2	2.0	18.6
MgO	0.7	2.7
CeO_2 – w/out reduction	0.8	0.9

Utilizing the Mo active site data, the CO STY for each material was determined by conducting a sweep of different space velocities (Fig. S3). To ensure that the supported catalysts were not limited by diffusion, the CO production rate at the three lowest residence times were chosen to generate a line of best fit, from which the y-intercept was used, along with the amount of Mo active sites and the total mass of catalyst, to calculate the CO STY values shown in Table 2. The STY values followed a similar trend to the CO_2 conversion rate with K-Mo_2C/Al_2O_3 exhibiting the highest CO STY of 55.6 min^{-1}. Both K-Mo_2C/SiO_2 and K-Mo_2C/ZrO_2 had similar values of 23.3 and 18.6 min^{-1}, respectively. MgO and CeO_2, which were found to have the lowest CO_2 conversions, were also found to have the lowest CO STY values. It is important to note that the STY values reported for K-Mo_2C/CeO_2 are for the sample that was not subjected to the hH_2 treatment. The STY values for the H_2 treated samples are not included as a realistic active site density could not be calculated by methods utilized herein for reasons discussed previously. As discussed in more detail below, the CO STY values shown in Table 2 indicate that the rate of CO production is dependent on the identity of the metal oxide support with non-reducible and more acidic oxides displaying higher STY values than reducible and basic oxides.

It has been previously demonstrated that the RWGS activity over metals such as Pt and Cu is greatly increased when supported on reducible oxides like CeO_2 and TiO_2.[26,71,73] However, our results appear to contrast with these trends as K-Mo_2C supported on the non-reducible oxides studied in this work are significantly more active than K-Mo_2C supported on reducible oxides. This outcome could be attributed to the different preparation methods employed for supported zero-valent metals compared to supported transition metal carbides. For instance, supported zero-valent metals are often calcined in air prior to testing.[71,73] This ensures that both the metal oxide support is fully oxidized and that any SMSI induced overlayer encapsulating the catalyst particles is also removed. However, in the case of supported transition metal carbides, this calcination step is infeasible as the desired carbide phase would readily transform into the corresponding oxide. Under the utilized preparation conditions for supported TMCs that involve high temperatures and reducing environments, reducible oxide supports are expected to have an increased number of oxygen vacancies and exhibit reduction of the cationic metal of the oxide.[46,66,74] This is believed to allow for electron transfer between the support and the deposited catalyst due to the SMSI. [66,74,75] This can help to rationalize the “over-reduction” of Mo_2C to metallic Mo on CeO_2. However, this phenomenon would be less impactful for the aforementioned supported zero-valent metals as the active phase is the fully reduced species. On the contrary, when Mo_2C is supported on non-reducible oxides such as Al_2O_3 or SiO_2, the carbide phase is stable and active for the RWGS.

As suggested by prior literature, our results also indicate that the acidity of the metal oxide support also appears to affect the measured catalytic activity.[50,53] Both γ-Al_2O_3 and ZrO_2 are generally considered to have prominent Lewis acid character. Furthermore, SiO_2 is classified as weakly acidic, MgO as basic, and CeO_2 has both weakly acidic and strongly basic properties.[76–78] The acidity of the support trends well with the CO STYs reported in Table 2 meaning that more acidic supports such as γ-Al_2O_3, SiO_2, and ZrO_2 have higher CO STYs than supports that are basic such as MgO. These acidic supports are thought to stabilize reaction intermediates including formates or carboxylates.[46,79] Conversely, MgO contains strong Lewis basic sites which heavily favors the adsorption of CO_2.[80,81] It is hypothesized that the strong interaction between the acidic CO_2 molecule and the basic MgO surface leads toward a Lewis acid-base adduct that inhibits the RWGS activity for Mo_2C catalysts and results in the low CO STYs observed. Finally, while CeO_2 is an amphoteric support and it is anticipated that the exposed acid sites do promote RWGS activity, the poor activity observed is likely attributed to the SMSI effects rather than the amphoteric nature of the CeO_2 support.

Prior studies have reported that molybdenum oxycarbide (Mo_2C-O) formed under operating conditions enhances the observed RWGS activity.[30,34,82,83] The formation of the Mo_2C-O is thought to arise from the interaction of CO_2 with Mo_2C which forms CO and the oxycarbide phase. The Mo_2C-O can then be reduced by H_2 to regenerate the Mo_2C surface with the concomitant formation of water.[30] To probe whether the evolution of Mo_2C to the oxycarbide species is not support dependent and that the observed TOF differences was due to the support acidity and reducibility, temperature programmed oxidation experiments coupled with mass spectrometry. Overall, no significant changes were observed in either the m/z = 44 or m/z = 28 (Fig. S4 f-i) signals which indicated that molybdenum oxycarbide had either not formed or was below the instrumental limit of detection. This corresponds well with prior reports that have indicated that only the first few surface layers of Mo_2C may undergo transformation to the oxycarbide as the bulk structure is thermodynamically unstable.[84] Further in-situ characterization methods would therefore be highly beneficial to fully understand any role the metal oxide support may have on the formation of a surface molybdenum oxycarbide phase.

To determine the stability of the supported Mo_2C catalysts under operating conditions, time on stream studies were conducted over the course of 13 hours for each catalyst at a WHSV of 2 mL s^{-1} g^{-1} and the results are presented in Fig. 4. While small decreases in the CO yield were initially observed for each material, the performance of each catalyst/support over 13 hours had minimal variations indicating that all 5 materials were stable. This corresponds well with prior reports from Juneau et al. and Sun et al. that demonstrated K-promoted Mo_2C/Al_2O_3 was stable under RWGS operating conditions for at least 10 days or 100 hours, respectively.[22,85]

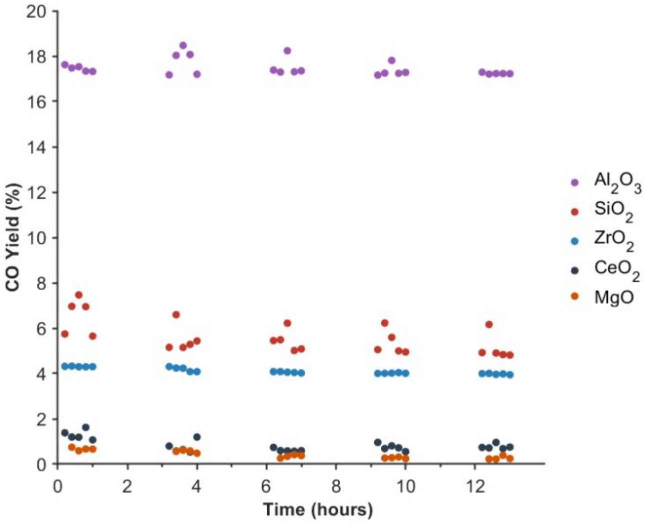

Fig. 4 Time on stream studies for K-promoted Mo_2C supported on various metal oxides at 300 °C and a WHSV of 2 mL s^{-1} g^{-1}.

DFT Modelling

DFT modelling was conducted to further probe supports effects on the adsorption energies of CO_2 and CO on Mo ribbons. In particular, MgO was selected as the model support due to its rocksalt structure and lattice parameter overlap with $Mo_2C(100)$. After relaxing the $Mo_2C(100)$ and MgO(111) slabs, CO_2 and CO were placed above both surfaces and allowed to relax with the resulting adsorption energies being tabulated in Table 3. For the $Mo_2C(100)$ slab, both CO_2 and CO adsorb to surface with energies of -1.63 and -2.66 eV, respectively (Fig. S5a and b). When CO_2 is placed above the bare MgO(111) surface (Fig. S5c), there is minimal interaction as indicated by an adsorption energy of -0.09 eV. Upon placing CO above the MgO(111) surface, it was observed that the CO molecule strips an oxygen from the MgO surface to form CO_2 (Fig. S5d) indicating that the formation of CO_2 was more favorable compared to the adsorption of CO. The calculated energy of this system was -5.6 eV though this was mainly attributed to the formation of the CO_2 molecule.

Table 3 Calculated CO_2 and CO adsorption energies from computational models of $Mo_2C(100)$, MgO(111), and Mo_2C/MgO. The * denotes two different CO adsorption configurations for Mo_2C/MgO(111).

	CO_2 Adsorption Energy (eV)	CO Adsorption Energy (eV)
$Mo_2C(100)$	-1.6	-2.7
MgO(111)	-0.09	-5.6
Mo_2C/MgO – a*	-0.9	-0.7
Mo_2C/MgO – b*	N.A.	-4.3

The $Mo_2C(100)$ and MgO(111) surfaces were then combined such that a ribbon of $Mo_2C(100)$ was attached to the surface of the MgO(111) slab. The optimal separation distance between the two slabs that resulted in the lowest "bulk" energy was determined to be approximately 1.5 Å. This separation distance was observed even when the Mo_2C and MgO slabs were initially separated by a distance of 4 Å. The calculated energies at various initial separation distances are presented in Fig. S6. To ensure that the Mo_2C ribbon and MgO slabs were electronically interacting at the selected separation distance of 1.8 Å, a charge density distribution (CDD) map was generated using VESTA and can be seen in Fig. S7.[86] The yellow surfaces represent areas of increased electron density while the blue surfaces represent areas of decreased electron energy. The CDD map demonstrates that there are significant electronic perturbations at the MgO/Mo_2C interface, indicating that the two slabs are not electronically isolated but are indeed interacting. Molecules of CO_2 and CO were then placed near the Mo_2C and MgO interface with the resulting adsorption energies being tabulated in Table 3. For CO_2, the adsorption energy was found to be -0.90 eV with an oxygen from CO_2 interacting with two Mo atoms in the Mo_2C ribbon and the carbon interacting with three oxygens, one of which is from the MgO surface layer (Fig. 5a). Interestingly, when CO was placed at the interface of Mo_2C/MgO and allowed to relax, two unique structures were observed. The first structure shows a bidentate adsorption to two surface O atoms with the O from the CO being stabilized by the Mo in the Mo_2C ribbon with an adsorption energy of -4.34

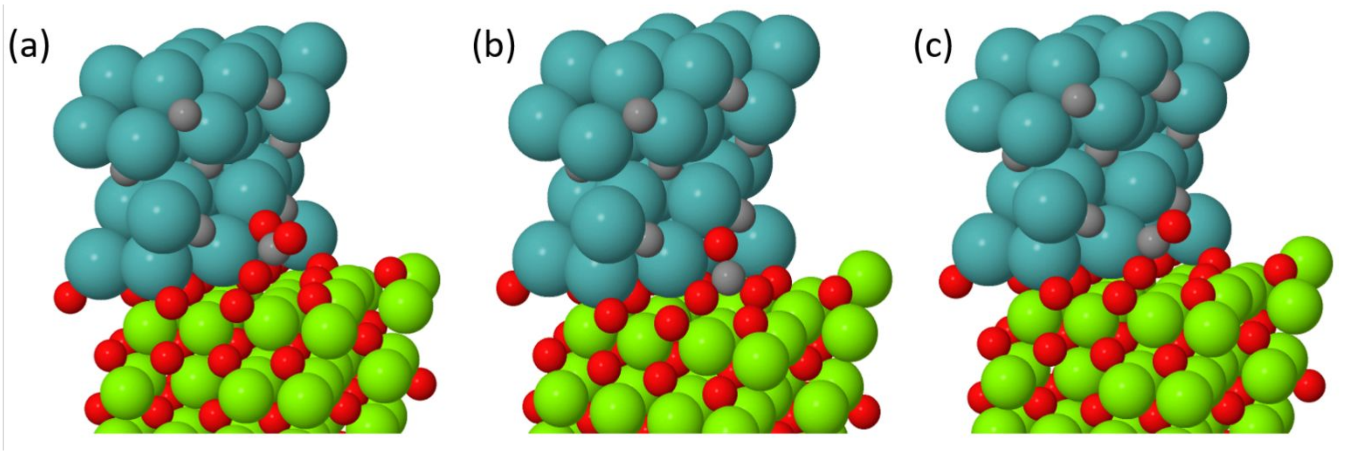

Fig. 5 Computation models depicting the adsorption of a) CO2 and b,c) CO at the Mo2C(100)/MgO(111) interface with green spheres representing Mg, red spheres representing O, blue spheres representing Mo, and gray spheres representing carbon.

eV (Fig. 5b). The second structure shows a monodentate adsorption of CO to the MgO surface with a less favorable adsorption energy of -0.66 eV (Fig. 5c).

From these results, it was concluded the adsorption energies of CO_2 and CO are markedly different when adsorbed at the Mo_2C/MgO interface when compared to the bulk MgO(111) or $Mo_2C(100)$ surfaces. For instance, the binding of CO_2 and CO to the pure $Mo_2C(100)$ slab showed favorable adsorption while on the MgO(111) surface, the adsorption was unfavorable for both adsorbates with the adsorbed CO molecule interacting with a lattice oxygen to form CO_2. However, when CO_2 and CO were placed at the Mo_2C/MgO interface, the adsorbates were found to interact with both surfaces. In particular, both adsorbates showed structures that contained a carbonate-like motif that interacted with the Mo_2C ribbon as well as the MgO support. The main difference between the two structures was that adsorbed CO interacted with two oxygens at the MgO surface while CO_2 only interacted with one surface MgO oxygen. This resulted in C-O bond distances that were on average shorter for the carbonate motif formed from CO than CO_2. Additionally, the shorter C-O bond distances also correlated well with significantly increased adsorption energies for CO (‘Mo_2C/MgO – a’ in Table 3) compared to CO_2. The large adsorption energies observed for CO at the interface in this arrangement could help to explain the poor experimental activity discussed in section 3.2 with the hypothesis that CO is strongly bound to the surface, which would inhibit catalytic activity. Therefore, the assumption that CO only adsorbs to the Mo sites in a 1:1 ratio may not be accurate for the Mo_2C/MgO system. Finally, CO was shown to have another unique structure when adsorbed at the Mo_2C/MgO interface which involved a monodentate binding of CO to the MgO surface. Unlike when CO was placed on the bulk MgO(111) surface, the calculated structure did not result with a MgO lattice oxygen being displaced from the surface to form CO_2. This implies that the nearby Mo_2C ribbon helps to stabilize the CO on the MgO surface, potentially through Mo-C interactions.

Further modelling is needed to systematically study how other low index facets of MgO such as the (110) and (100) interact with ribbons of Mo_2C on the surface as well as the influence these facets may have on the adsorption of CO_2 and CO. Furthermore, expansion to other oxide support systems could help to elucidate the role of the support in influencing the RWGS activity observed for Mo_2C.

Conclusions

Potassium promoted molybdenum carbide was supported on various metal oxides to determine the role that support acidity and reducibility have on the RWGS activity. To accurately compare the materials against each other, the CO STY normalized for the Mo active site density was determined for each catalyst/support system. Our results indicated that CO STYs are greater for K-Mo_2C when supported on acidic, non-reducible metal oxides while reducible oxide supports do not lead to greater CO STY’s for K-Mo_2C. For instance, supports that contained acidic sites such as γ-Al_2O_3 or ZrO_2 were considerably more active than those containing numerous basic sites like MgO. Meanwhile, when K-Mo_2C was supported on a reducible support such as CeO_2, the Mo_2C was over-reduced to metallic Mo which significantly hindered the observed RWGS activity. Accordingly, the non-reducible and Lewis acidic support γ-Al_2O_3, was determined to be the best performing metal oxide support of those studied herein, for the K-Mo_2C catalyst with a CO STY of 55.6 min^{-1}. Finally, computational modelling for Mo_2C supported on MgO provided insights into the low activity observed over the catalyst. When CO is adsorbed at the interface, the formation of a carbonate-like motif was observed, leading to the hypothesis that CO may be poisoning active sites of the K-Mo_2C/MgO catalyst which further explains the poor activity. Additional investigations are currently underway that utilize DFT modelling to further understand support effects and their influence on the K-Mo_2C RWGS activity.

Author Contributions

Cameron F. Holder – Conceptualization, Methodology, Writing – original draft, Writing – review and editing, Funding. **James. R. Morse** – Conceptualization, Writing – review and editing. **Patrick M. Barboun** – Writing – review and editing. **Andrew R. Shabaev** – Methodology. **Jeffrey W. Baldwin** – Supervision. **Heather D. Willauer** – Funding acquisition, Supervision, Writing – review and editing.

Conflicts of interest

The authors declare that they have no known competing financial or personal interest that may have influenced the results presented in this paper.

Acknowledgements

The authors are thankful to the U.S. Naval Research Laboratory, and the Office of Naval Research for financial support.

References

1 J. A. Turner, *Science*, 1999, **285**, 687–689.

2 N. S. Lewis and D. G. Nocera, *Proc. Natl. Acad. Sci.*, 2006, **103**, 15729–15735.

3 B. Yu and L.-N. He, *ChemSusChem*, 2015, **8**, 52–62.

4 J. Keasling, H. Garcia Martin, T. S. Lee, A. Mukhopadhyay, S. W. Singer and E. Sundstrom, *Nat. Rev. Microbiol.*, 2021, **19**, 701–715.

5 P. Mehta, P. Barboun, F. A. Herrera, J. Kim, P. Rumbach, D. B. Go, J. C. Hicks and W. F. Schneider, *Nat. Catal.*, 2018, **1**, 269–275.

6 W.-H. Wang, Y. Himeda, J. T. Muckerman, G. F. Manbeck and E. Fujita, *Chem. Rev.*, 2015, **115**, 12936–12973.

7 M. D. Porosoff, B. Yan and J. G. Chen, *Energy Environ. Sci.*, 2016, **9**, 62–73.

8 S. Nitopi, E. Bertheussen, S. B. Scott, X. Liu, A. K. Engstfeld, S. Horch, B. Seger, I. E. L. Stephens, K. Chan, C. Hahn, J. K. Nørskov, T. F. Jaramillo and I. Chorkendorff, *Chem. Rev.*, 2019, **119**, 7610–7672.

9 2021, **86**, 70935–70943.

10 U.S. Department of Defense, 2021, 1–32.

11 H. D. Willauer, F. DiMascio, D. R. Hardy and F. W. Williams, *Energy and Fuels*, 2017, **31**, 1723–1730.

12 H. D. Willauer, F. DiMascio, D. R. Hardy, M. K. Lewis and F. W. Williams, *Ind. Eng. Chem. Res.*, 2011, **50**, 9876–9882.

13 H. D. Willauer, F. DiMascio, D. R. Hardy, M. K. Lewis and F. W. Williams, *Ind. Eng. Chem. Res.*, 2012, **51**, 11254–11260.

14 H. D. Willauer, F. DiMascio, D. R. Hardy and F. W. Williams, *Ind. Eng. Chem. Res.*, 2014, **53**, 12192–12200.

15 H. D. Willauer, D. R. Hardy, M. K. Lewis, E. C. Ndubizu and F. W. Williams, *Energy & Fuels*, 2010, **24**, 6682–6688.

16 M. D. Porosoff, J. W. Baldwin, X. Peng, G. Mpourmpakis and H. D. Willauer, *ChemSusChem*, 2017, **10**, 2408–2415.

17 J. R. Morse, M. Juneau, J. W. Baldwin, M. D. Porosoff and H. D. Willauer, *J. CO2 Util.*, 2020, **35**, 38–46.

18 M. V. Twigg, *Catalyst Handbook*, 2nd edn., 1989.

19 H.-X. Liu, S.-Q. Li, W.-W. Wang, W.-Z. Yu, W.-J. Zhang, C. Ma and C.-J. Jia, *Nat. Commun.*, 2022, **13**, 867.

20 X. Zhang, X. Zhu, L. Lin, S. Yao, M. Zhang, X. Liu, X. Wang, Y.-W. Li, C. Shi and D. Ma, *ACS Catal.*, 2017, **7**, 912–918.

21 C.-S. Chen, W.-H. Cheng and S.-S. Lin, *Appl. Catal. A Gen.*, 2004, **257**, 97–106.

22 M. Juneau, M. Vonglis, J. Hartvigsen, L. Frost, D. Bayerl, M. Dixit, G. Mpourmpakis, J. R. Morse, J. W. Baldwin, H. D. Willauer and M. D. Porosoff, *Energy Environ. Sci.*, 2020, **13**, 2524–2539.

23 X. Chen, X. Su, H.-Y. Su, X. Liu, S. Miao, Y. Zhao, K. Sun, Y. Huang and T. Zhang, *ACS Catal.*, 2017, **7**, 4613–4620.

24 R. M. Bown, M. Joyce, Q. Zhang, T. R. Reina and M. S. Duyar, *Energy Technol.*, 2021, **9**, 2100554.

25 T. Wang, M. D. Porosoff and J. G. Chen, *Catal. Today*, 2014, **233**, 61–69.

26 S. Kattel, B. Yan, J. G. Chen and P. Liu, *J. Catal.*, 2016, **343**, 115–126.

27 J. Ye, Q. Ge and C. Liu, *Chem. Eng. Sci.*, 2015, **135**, 193–201.

28 J. H. Kwak, L. Kovarik and J. Szanyi, *ACS Catal.*, 2013, **3**, 2094–2100.

29 R. B. Levy and M. Boudart, *Science*, 1973, **181**, 547–549.

30 M. D. Porosoff, X. Yang, J. A. Boscoboinik and J. G. Chen, *Angew. Chemie Int. Ed.*, 2014, **53**, 6705–6709.

31 P. Liu and J. A. Rodriguez, *J. Phys. Chem. B*, 2006, **110**, 19418–19425.

32 H. Zhou, Z. Chen, E. Kountoupi, A. Tsoukalou, P. M. Abdala, P. Florian, A. Fedorov and C. R. Müller, *Nat. Commun.*, 2021, **12**, 5510.

33 S. Posada-Pérez, F. Viñes, P. J. Ramirez, A. B. Vidal, J. A. Rodriguez and F. Illas, *Phys. Chem. Chem. Phys.*, 2014, **16**, 14912–14921.

34 A. Kurlov, E. B. Deeva, P. M. Abdala, D. Lebedev, A. Tsoukalou, A. Comas-Vives, A. Fedorov and C. R. Müller, *Nat. Commun.*, 2020, **11**, 4920.

35 C. G. Silva, F. B. Passos and V. T. da Silva, *J. Catal.*, 2019, **375**, 507–518.

36 S. B. Derouane-Abd Hamid, J. R. Anderson, I. Schmidt, C. Bouchy, C. J. H. Jacobsen and E. G. Derouane, *Catal. Today*, 2000, **63**, 461–469.

37 F. Solymosi, J. Cserényi, A. Szöke, T. Bánsági and A. Oszkó, *J. Catal.*, 1997, **165**, 150–161.

38 H. Vrubel and X. Hu, *Angew. Chemie Int. Ed.*, 2012, **51**, 12703–12706.

39 C. Wan, Y. N. Regmi and B. M. Leonard, *Angew. Chemie Int. Ed.*, 2014, **53**, 6407–6410.

40 C. Panaritis, M. Edake, M. Couillard, R. Einakchi and E. A. Baranova, *J. CO2 Util.*, 2018, **26**, 350–358.

41 D. L. Jurković, A. Pohar, V. D. B. C. Dasireddy and B. Likozar, *Chem. Eng. Technol.*, 2017, **40**, 973–980.

42 I. Chorkendorff and J. W. Niemantsverdriet, *Concepts of Moden Catalysis and Kinetics*, Wiley-VCH Verlag, 2003.

43 M. Zhu, Q. Ge and X. Zhu, *Trans. Tianjin Univ.*, 2020, 26, 172–187.

44 S. J. Tauster, S. C. Fung and R. L. Garten, *J. Am. Chem. Soc.*, 1978, **100**, 170–175.

45 A. Goguet, F. C. Meunier, D. Tibiletti, J. P. Breen and R. Burch, *J. Phys. Chem. B*, 2004, **108**, 20240–20246.

46 L. F. Bobadilla, J. L. Santos, S. Ivanova, J. A. Odriozola and A. Urakawa, *ACS Catal.*, 2018, **8**, 7455–7467.

47 C.-S. Chen, W.-H. Cheng and S.-S. Lin, *Catal. Letters*, 2000, **68**, 45–48.

48 M. J. L. Ginés, A. J. Marchi and C. R. Apesteguía, *Appl. Catal. A Gen.*, 1997, **154**, 155–171.

49 M. Miyamoto, A. Hamajima, Y. Oumi and S. Uemiya, *Int. J. Hydrogen Energy*, 2018, **43**, 730–738.

50 F. Saad, J. D. Comparot, R. Brahmi, M. Bensitel and L. Pirault-Roy, *Appl. Catal. A Gen.*, 2017, **544**, 1–9.

51 C. Leyva, M. S. Rana, F. Trejo and J. Ancheyta, *Ind. Eng. Chem. Res.*, 2007, **46**, 7448–7466.

52 J. Zhao, H. Chen, J. Xu and J. Shen, *J. Phys. Chem. C*, 2013, **117**, 10573–10580.

53 M. Juneau, C. Pope, R. Liu and M. D. Porosoff, *Appl. Catal. A Gen.*, 2021, **620**, 118034.

54 H. Sakurai, S. Tsubota and M. Haruta, *Appl. Catal. A Gen.*, 1993, **102**, 125–136.

55 J. S. Lee, S. T. Oyama and M. Boudart, *J. Catal.*, 1987, **106**, 125–133.

56 J. S. Lee, K. H. Lee and J. Y. Lee, *J. Phys. Chem.*, 1992, **96**, 362–366.

57 G. Kresse and J. Furthmüller, *Phys. Rev. B - Condens. Matter Mater. Phys.*, 1996, **54**, 11169–11186.

58 J. P. Perdew, K. Burke and M. Ernzerhof, *Phys. Rev. Lett.*, 1996, **77**, 3865–3868.

59 P. E. Blöchl, *Phys. Rev. B*, 1994, **50**, 17953–17979.

60 H. J. Monkhorst and J. D. Pack, *Phys. Rev. B*, 1976, **13**, 5188–5192.

61 T. Xiao, A. P. E. York, V. C. Williams, H. Al-Megren, A. Hanif, X. Zhou and M. L. H. Green, *Chem. Mater.*, 2000, **12**, 3896–3905.

62 S. Li, W. B. Kim and J. S. Lee, *Chem. Mater.*, 1998, **10**, 1853–1862.

63 C. G. Vayenas, S. Brosda and C. Pliangos, *J. Catal.*, 2003, **216**, 487–504.

64 J. Disdier, J.-M. Herrmann and P. Pichat, *J. Chem. Soc. Faraday Trans. 1 Phys. Chem. Condens. Phases*, 1983, **79**, 651–660.

65 Q. Fu, T. Wagner, S. Olliges and H.-D. Carstanjen, *J. Phys. Chem. B*, 2005, **109**, 944–951.

66 S. J. Tauster, S. C. Fung, R. T. K. Baker and J. A. Horsley, *Science*, 1981, **211**, 1121–1125.

67 X. Liu, C. Kunkel, P. Ramírez de la Piscina, N. Homs, F. Viñes and F. Illas, *ACS Catal.*, 2017, **7**, 4323–4335.

68 J. W. Han, L. Li and D. S. Sholl, *J. Phys. Chem. C*, 2011, **115**, 6870–6876.

69 I. Szenti, L. Bugyi and Z. Kónya, *Surf. Sci.*, 2015, **641**, 60–67.

70 B. Domenichini, G. Andrea Rizzi, P. Krüger, M. Della Negra, Z. Li, M. Petukhov, G. Granozzi, P. Juul Møller and S. Bourgeois, *Phys. Rev. B*, 2006, **73**, 245433.

71 S. S. Kim, K. H. Park and S. C. Hong, *Fuel Process. Technol.*, 2013, **108**, 47–54.

72 A. G. Kharaji, A. Shariati and M. A. Takassi, *Chinese J. Chem. Eng.*, 2013, **21**, 1007–1014.

73 S.-C. Yang, S. H. Pang, T. P. Sulmonetti, W.-N. Su, J.-F. Lee, B.-J. Hwang and C. W. Jones, *ACS Catal.*, 2018, **8**, 12056–12066.

74 E. W. Zhao, H. Zheng, K. Ludden, Y. Xin, H. E. Hagelin-Weaver and C. R. Bowers, *ACS Catal.*, 2016, **6**, 974–978.

75 A. Ruiz Puigdollers, P. Schlexer, S. Tosoni and G. Pacchioni, *ACS Catal.*, 2017, **7**, 6493–6513.

76 M. Kumar, F. Aberuagba, J. K. Gupta, K. S. Rawat, L. D. Sharma and G. Murali Dhar, *J. Mol. Catal. A Chem.*, 2004, **213**, 217–223.

77 M. K. Gnanamani, R. Garcia, G. Jacobs, K. Góra-Marek, D. C. Cronauer, A. J. Kropf and C. L. Marshall, *Appl. Catal. A Gen.*, 2020, **602**, 117722.

78 J. J. Corral-Pérez, C. Copéret and A. Urakawa, *J. Catal.*, 2019, **380**, 153–160.

79 A. A. Upadhye, I. Ro, X. Zeng, H. J. Kim, I. Tejedor, M. A. Anderson, J. A. Dumesic and G. W. Huber, *Catal. Sci. Technol.*, 2015, **5**, 2590–2601.

80 P. Hu, S. Wang and Y. Zhuo, *Sep. Purif. Technol.*, 2022, **284**, 120253.

81 A. O. Menezes, P. S. Silva, E. Padrón Hernández, L. E. P. Borges and M. A. Fraga, *Langmuir*, 2010, **26**, 3382–3387.

82 A. Kurlov, X. Huang, E. B. Deeva, P. M. Abdala, A. Fedorov and C. R. Müller, *Nanoscale*, 2020, **12**, 13086–13094.

83 A. Kurlov, D. Stoian, A. Baghizadeh, E. Kountoupi, E. B. Deeva, M. Willinger, P. M. Abdala, A. Fedorov and C. R. Müller, *Catal. Sci. Technol.*, 2022, **12**, 5620–5628.

84 S. R. J. Likith, C. A. Farberow, S. Manna, A. Abdulslam, V. Stevanović, D. A. Ruddy, J. A. Schaidle, D. J. Robichaud and C. V Ciobanu, *J. Phys. Chem. C*, 2018, **122**, 1223–1233.

85 G. Sun, S. Mottaghi-Tabar, L. Ricardez-Sandoval and D. S. A. Simakov, *Top. Catal.*, 2021, **64**, 414–430.

86 K. Momma and F. Izumi, *J. Appl. Crystallogr.*, 2011, **44**, 1272–1276.